

# Wave-equation tomography using image-space phase-encoded data

*Claudio Guerra, Yaxun Tang, and Biondo Biondi*

## ABSTRACT

Wave-equation tomography in the image-space is a powerful technique that promises to yield more reliable velocity models than ray-based migration velocity analysis in areas of complex overburden. Its practical use, however, is limited because of the high computational cost. Applying a target-oriented approach and using data reduction can make wave-equation tomography in the image space of practical use. Here, we present results of applying image-space wave-equation tomography in the generalized source domain, where a small number of synthesized shot gathers are generated. Specifically, we generate synthesized shot gathers by image-space phase encoding. This technique can also be used in a target-oriented way. The comparison of the gradients of the tomography objective functional obtained using image-space encoded gathers with those obtained using the original shot gathers shows that those encoded shot gathers can be used in wave-equation tomography problems. Velocity inversion using image-space phase-encoded gathers converges to reasonable results when compared to the correct velocity model. We illustrate our method by applying it to the Marmousi model.

## INTRODUCTION

Wave-equation tomography has the potential to overcome the problems faced by ray-based traveltimes tomography when estimating the velocity model in complex geological scenarios. This is because wave-equation tomography uses band-limited wavefields instead of infinite-frequency rays as carriers of information; thus it is robust even in the presence of strong velocity contrasts and immune to multi-pathing issues. However, despite its theoretical advantages, wave-equation tomography is still computationally challenging. In the shot-profile domain, for instance, every wave-equation tomography iteration costs as much as three prestack wave-equation migrations.

Wave-equation tomography can be performed in the data-space domain (Tarantola, 1987; Woodward, 1992) or in the image-space domain (Biondi and Sava, 1999; Shen, 2004). The image-space approach minimizes the residual in the image domain obtained after migration. Regardless of the domain of application, using phase-encoded data can substantially decrease the computational cost of wave-equation tomography (Vigh and Starr, 2008; Shen and Symes, 2008). Tang et al. (2008) extended the theory of image-space wave-equation tomography from the conventional

shot-profile domain (Shen, 2004) to the generalized source domain. The generalized source domain can be obtained in two different spaces. In the data-space, shot gathers are combined and the corresponding source function is synthesized, using a convenient phase-encoding scheme, which characterizes the data-space phase encoding (Whitmore, 1995; Romero et al., 2000). In the image-space, source- and receiver-areal data are synthesized by upward propagating wavefields, having as the initial condition a prestack image computed with wave-equation migration, according to the prestack exploding-reflector modeling (Biondi, 2006, 2007). The modeling experiments can be combined such that a small quantity of areal data is generated, characterizing the image-space phase encoding (Guerra and Biondi, 2008).

In this paper, we show that image-space phase-encoded wavefields can be used to estimate the velocity model in image-space wave-equation tomography. We show that the gradient of the tomographic objective functional is similar to that obtained in the original shot-profile domain, but with less computational cost. Velocity inversion using image-space phase-encoded gathers converges to reasonable results when compared to the correct velocity model, provided that crosstalk has been sufficiently attenuated. We briefly discuss the theory of wave-equation tomography in the image-space domain; then we explain the prestack exploding-reflector modeling and show that the image-space phase encoding can be used to accelerate wave-equation tomography in the image domain. We use the Marmousi model to illustrate the method.

## IMAGE-SPACE WAVE-EQUATION TOMOGRAPHY

Image-space wave-equation tomography is a non-linear inverse problem that tries to find an optimal background slowness that minimizes the residual field,  $\Delta\mathbf{I}$ , defined in the image space. The residual field is derived from the background image,  $\mathbf{I}$ , which is computed with a background slowness. The general form of the residual field is (Biondi, 2008)

$$\Delta\mathbf{I} = \mathbf{I} - \mathbf{F}(\mathbf{I}), \quad (1)$$

where  $\mathbf{F}$  is a focusing operator, which measures the focusing of the migrated image. In particular, in the Differential Semblance Optimization (DSO) method (Shen, 2004), the focusing operator takes the form:

$$\mathbf{F}(\mathbf{I}) = (\mathbf{1} - \mathbf{O})\mathbf{I}, \quad (2)$$

where  $\mathbf{1}$  is the identity operator and  $\mathbf{O}$  is the DSO operator either in the subsurface offset domain or in the angle domain (Shen, 2004).

Under  $\ell_2$  norm, the tomography objective function can be written as follows:

$$J = \frac{1}{2} \|\Delta\mathbf{I}\|_2^2 = \frac{1}{2} \|\mathbf{I} - \mathbf{F}(\mathbf{I})\|_2^2. \quad (3)$$

The gradient of  $J$  with respect to the slowness  $\mathbf{s}$  is

$$\nabla J = \left( \frac{\partial\mathbf{I}}{\partial\mathbf{s}} - \frac{\partial\mathbf{F}(\mathbf{I})}{\partial\mathbf{s}} \right)^* (\mathbf{I} - \mathbf{F}(\mathbf{I})), \quad (4)$$

where  $*$  denotes the adjoint.

The adjoint of the linear operator  $\frac{\partial \mathbf{I}}{\partial \mathbf{s}} \Big|_{\mathbf{s}=\widehat{\mathbf{s}}}$ , which defines a linear mapping from the slowness perturbation  $\Delta \mathbf{s}$  to the image perturbation  $\Delta \mathbf{I}$ , can be computed by expanding the image  $\mathbf{I}$  around the background slowness  $\widehat{\mathbf{s}}$ . Keeping only the zeroth and first order terms, we get the linear operator  $\frac{\partial \mathbf{I}}{\partial \mathbf{s}} \Big|_{\mathbf{s}=\widehat{\mathbf{s}}}$  as follows:

$$\Delta \mathbf{I} = \frac{\partial \mathbf{I}}{\partial \mathbf{s}} \Big|_{\mathbf{s}=\widehat{\mathbf{s}}} \Delta \mathbf{s} = \mathbf{T} \Delta \mathbf{s}, \quad (5)$$

where  $\Delta \mathbf{I} = \mathbf{I} - \widehat{\mathbf{I}}$ ,  $\widehat{\mathbf{I}}$  is the background image computed with the background slowness  $\widehat{\mathbf{s}}$  and  $\Delta \mathbf{s} = \mathbf{s} - \widehat{\mathbf{s}}$ .  $\mathbf{T} = \frac{\partial \mathbf{I}}{\partial \mathbf{s}} \Big|_{\mathbf{s}=\widehat{\mathbf{s}}}$  is the wave-equation tomographic operator. The tomographic operator can be evaluated either in the source and receiver domain (Sava, 2004) or in the shot-profile domain (Shen, 2004).

In the shot-profile domain, both source and receiver wavefields are downward continued with the one-way wave equation (Claerbout, 1971), and the image is computed by applying the cross-correlation imaging condition:

$$I(\mathbf{x}, \mathbf{h}) = \sum_{\mathbf{x}_s} \sum_{\omega} \overline{D(\mathbf{x} - \mathbf{h}, \mathbf{x}_s, \omega)} U(\mathbf{x} + \mathbf{h}, \mathbf{x}_s, \omega), \quad (6)$$

where  $D(\mathbf{x}, \mathbf{x}_s, \omega)$  is the source wavefield for a single frequency  $\omega$  at image point  $\mathbf{x} = (x, y, z)$  with the source located at  $\mathbf{x}_s = (x_s, y_s, 0)$ ;  $U(\mathbf{x}, \mathbf{x}_s, \omega)$  is the receiver wavefield and  $\mathbf{h} = (h_x, h_y, h_z)$  is the subsurface half-offset. The overline represents the complex conjugate.

The perturbed image can be derived by the application of the chain rule to Equation 6:

$$\Delta I(\mathbf{x}, \mathbf{h}) = \sum_{\mathbf{x}_s} \sum_{\omega} \left( \overline{\Delta D(\mathbf{x} - \mathbf{h}, \mathbf{x}_s, \omega)} \widehat{U}(\mathbf{x} + \mathbf{h}, \mathbf{x}_s, \omega) + \overline{\widehat{D}(\mathbf{x} - \mathbf{h}, \mathbf{x}_s, \omega)} \Delta U(\mathbf{x} + \mathbf{h}, \mathbf{x}_s, \omega) \right), \quad (7)$$

where  $\widehat{D}(\mathbf{x} - \mathbf{h}, \mathbf{x}_s, \omega)$  and  $\widehat{U}(\mathbf{x} + \mathbf{h}, \mathbf{x}_s, \omega)$  are the background source and receiver wavefields computed with the background slowness  $\widehat{\mathbf{s}}(\mathbf{x})$ ;  $\Delta D(\mathbf{x} - \mathbf{h}, \mathbf{x}_s, \omega)$  and  $\Delta U(\mathbf{x} + \mathbf{h}, \mathbf{x}_s, \omega)$  are the perturbed source wavefield and perturbed receiver wavefield, which are the results of the slowness perturbation  $\Delta \mathbf{s}(\mathbf{x})$ . The perturbed source and receiver wavefields satisfy the perturbed one-way wave equation (Shen, 2004).

To evaluate the adjoint tomographic operator  $\mathbf{T}^*$ , we first apply the adjoint of the imaging condition in Equation 7 to get the perturbed source and receiver wavefields  $\Delta D(\mathbf{x}, \mathbf{x}_s, \omega)$  and  $\Delta U(\mathbf{x}, \mathbf{x}_s, \omega)$  as follows:

$$\Delta D(\mathbf{x}, \mathbf{x}_s, \omega) = \sum_{\mathbf{h}} \Delta I(\mathbf{x}, \mathbf{h}) \widehat{U}(\mathbf{x} + \mathbf{h}, \mathbf{x}_s, \omega), \quad (8)$$

$$\Delta U(\mathbf{x}, \mathbf{x}_s, \omega) = \sum_{\mathbf{h}} \Delta I(\mathbf{x}, \mathbf{h}) \widehat{D}(\mathbf{x} - \mathbf{h}, \mathbf{x}_s, \omega). \quad (9)$$

Then we solve the adjoint perturbed one-way wave equation to get the slowness perturbation  $\Delta s(\mathbf{x})$  (Shen, 2004). More detailed information on how to evaluate the forward and adjoint operators can be found in Tang et al. (2008).

## PRESTACK EXPLODING-REFLECTOR MODELING

The general idea of prestack exploding-reflector modeling (Biondi, 2006) is to model the data and corresponding source function that are related to only one event in the subsurface. In this case, a single unfocused subsurface-offset-domain common-image gather (SODCIG) containing a single reflector is used as the initial condition for recursive upward continuation with the following one-way wave equations:

$$\begin{cases} \left( \frac{\partial}{\partial z} - i\Lambda \right) Q_D(\mathbf{x}, \omega; x_m, y_m) = I_D(\mathbf{x}, \mathbf{h}; x_m, y_m) \\ Q_D(x, y, z = z_{\max}, \omega; x_m, y_m) = 0 \end{cases}, \quad (10)$$

and

$$\begin{cases} \left( \frac{\partial}{\partial z} - i\Lambda \right) Q_U(\mathbf{x}, \omega; x_m, y_m) = I_U(\mathbf{x}, \mathbf{h}; x_m, y_m) \\ Q_U(x, y, z = z_{\max}, \omega; x_m, y_m) = 0 \end{cases}, \quad (11)$$

where  $I_D(\mathbf{x}, \mathbf{h}; x_m, y_m)$  and  $I_U(\mathbf{x}, \mathbf{h}; x_m, y_m)$  are the isolated SODCIGs at the horizontal location  $(x_m, y_m)$  for a single reflector, and are suitable for the initial conditions for the source and receiver wavefields, respectively. As Biondi (2006) discusses, a rotation of the image gathers according to the apparent geological dip must be performed prior to modeling. By collecting the wavefields at the surface, we obtain the areal source data  $Q_D(x, y, z = 0, \omega; x_m, y_m)$  and the areal receiver data  $Q_U(x, y, z = 0, \omega; x_m, y_m)$  for a single reflector and a single SODCIG located at  $(x_m, y_m)$ .  $\Lambda$  is the square-root operator defined by

$$\Lambda = \sqrt{\omega^2 \hat{s}^2(\mathbf{x}) - |\mathbf{k}|^2},$$

where  $s(\mathbf{x})$  is the slowness at  $\mathbf{x}$  and  $\mathbf{k} = (k_x, k_y)$  is the spatial wavenumber vector.

Since the size of the migrated image volume can be very big in practice, and there are usually many reflectors in the subsurface, modeling each reflector and each SODCIG may generate a data set even bigger than the original data set. One strategy to reduce the cost is to model several reflectors and several SODCIGs simultaneously (Biondi, 2006); however, this process generates unwanted crosstalk. As discussed by Guerra and Biondi (2008), random phase encoding can be used to attenuate the crosstalk.

One important characteristic of the prestack exploding reflector modeling is that, for velocity model building, the wavefields can be upward propagated to a certain depth level or depth horizon, provided that the velocity model above is sufficiently accurate. Therefore, a target-oriented strategy can be applied to derive the velocity model below the that depth.

## IMAGE-SPACE PHASE-ENCODED WAVEFIELDS

The randomly encoded areal source and areal receiver wavefields can be computed as follows:

$$\begin{cases} \left(\frac{\partial}{\partial z} - i\Lambda\right) \tilde{Q}_D(\mathbf{x}, \mathbf{p}_m, \omega) = \tilde{I}_D(\mathbf{x}, \mathbf{h}, \mathbf{p}_m, \omega) \\ \tilde{Q}_D(x, y, z = z_{\max}, \mathbf{p}_m, \omega) = 0 \end{cases}, \quad (12)$$

and

$$\begin{cases} \left(\frac{\partial}{\partial z} - i\Lambda\right) \tilde{Q}_U(\mathbf{x}, \mathbf{p}_m, \omega) = \tilde{I}_U(\mathbf{x}, \mathbf{h}, \mathbf{p}_m, \omega) \\ \tilde{Q}_U(x, y, z = z_{\max}, \mathbf{p}_m, \omega) = 0 \end{cases}, \quad (13)$$

where  $\tilde{I}_D(\mathbf{x}, \mathbf{h}, \mathbf{p}_m, \omega)$  and  $\tilde{I}_U(\mathbf{x}, \mathbf{h}, \mathbf{p}_m, \omega)$  are the encoded SODCIGs. They are defined as:

$$\begin{aligned} \tilde{I}_D(\mathbf{x}, \mathbf{h}, \mathbf{p}_m, \omega) &= \sum_{x_m, y_m} I_D(\mathbf{x}, \mathbf{h}, x_m, y_m) \beta, \\ \tilde{I}_U(\mathbf{x}, \mathbf{h}, \mathbf{p}_m, \omega) &= \sum_{x_m, y_m} I_U(\mathbf{x}, \mathbf{h}, x_m, y_m) \beta, \end{aligned} \quad (14)$$

where  $\beta = e^{i\gamma(\mathbf{x}, x_m, y_m, \mathbf{p}_m, \omega)}$  is chosen to be the random phase-encoding function, with  $\gamma(\mathbf{x}, x_m, y_m, \mathbf{p}_m, \omega)$  being a uniformly distributed random sequence in  $\mathbf{x}$ ,  $x_m$ ,  $y_m$  and  $\omega$ ; the variable  $\mathbf{p}_m$  is the index of different realizations of the random sequence. Recursively solving Equations 12 and 13 gives us the encoded areal source data  $\tilde{Q}_D(x, y, z = 0, \mathbf{p}_m, \omega)$  and encoded areal receiver data  $\tilde{Q}_U(x, y, z = 0, \mathbf{p}_m, \omega)$ , which can be collected at any depth.

In image-space wave-equation tomography, the image-space phase-encoded areal data sets are downward continued using the one-way wave equation. The background image is produced by cross-correlating the two wavefields and summing images for all realizations  $\mathbf{p}_m$ , as follows:

$$I_{\text{me}}(\mathbf{x}, \mathbf{h}) = \sum_{\mathbf{p}_m, \omega} \overline{\tilde{D}(\mathbf{x}, \mathbf{p}_m, \omega)} \tilde{U}(\mathbf{x}, \mathbf{p}_m, \omega). \quad (15)$$

The initial condition for modeling simultaneous events is set by regularly selecting SODCIGs in the prestack image. The amount of crosstalk in the image  $I_{\text{me}}(\mathbf{x}, \mathbf{h})$  can be controlled by choosing a convenient sampling interval for SODCIGs used simultaneously for the modeling. For instance, if only one reflector is present and the correct velocity is used, no crosstalk is generated if the SODCIG interval is greater than twice the maximum subsurface offset of the prestack image. In the extreme case, when an incorrect velocity is used and the reflector's energy spreads through the whole range of subsurface offsets, crosstalk is not generated if the the SODCIG interval is greater than four times the maximum subsurface offset. In the presence of more than one reflector, crosstalk between reflectors occurs, regardless of the distance between SODCIGs input to modeling. By phase-encoding the reflectors, we can mitigate the crosstalk.

To phase-encode the reflectors, however, it is necessary to pick some significant reflectors in the prestack migrated data. This implies a horizon-based approach for the prestack exploding-reflector modeling. In velocity-model updating, the idea of using some key reflectors to extract the residual-moveout information is an established strategy (Stork, 1992; Kosloff et al., 1996; Jiao et al., 2008).

The perturbed image is obtained by applying the chain rule to Equation 15. The slowness perturbation is computed by applying the adjoint of the tomographic operator,  $\mathbf{T}^*$ , to the image perturbation.

## NUMERICAL EXAMPLES

We test the image-space wave-equation tomography using image-space encoded data on a smoothed version of the Marmousi model, computed by applying a 200 m 2D-median filter to the slowness model. One-way data were synthesized considering a reflectivity computed from the Marmousi stratigraphic velocity model. We modeled 376 shots, ranging from 0 to 9000 m, with 24 m spacing. We used split-spread acquisition geometry, with maximum offset of 6600 m and receiver spacing of 24 m.

Figure 1(a) shows the true slowness model. The background velocity model is equal to the correct velocity model above 2400 m depth and above the anticline with apex at ( $x = 6000$  m,  $z = 1850$  m). Therefore, the slowness perturbation is zero in this portion of the model. Below these horizons, the background model is characterized by a smoother version of the original Marmousi model, computed with a 400 m 2D-median filter and scaled down by a factor of 5%. Figure 1(b) shows the background slowness. By using this background slowness model, we assume that the slowness model has been already defined up to a certain horizon, as usually occurs in projects of velocity model building. The slowness perturbation, computed by taking the difference between the correct and background slownesses, is shown in Figure 2(a). In the part where the slowness perturbation is different from zero, the ratio between the true and the background slowness ranges approximately from 0.8 to 0.92 (Figure 2(b)). Notice that the minimum depth is 1500 m. Henceforth, all the figures will be displayed with a minimum depth of 1500 m.

To compute the image-space phase-encoded data, we picked 10 reflectors in the non-zero slowness perturbation part, in the prestack image computed with the 376 original shots using the background slowness model. Figure 3 shows the background image (Figure 3a) computed with shot-profile migration. The panel on the left corresponds to the zero-subsurface-offset section, and the panel on the right is the SODCIG at CMP position 5500 m. Notice the effects of using an inaccurate background slowness. The reflector at (7000 m, 2500 m) is pulled up, as are the subjacent reflectors. In the SODCIG, the energy is not focused at the zero subsurface offset.

Figure 3(b) shows the picked reflectors used to model the image-space phase-encoded data. This image is used as input for the rotation of the reflectors in the SODCIGs with respect to the apparent geological dip, and the results are used as

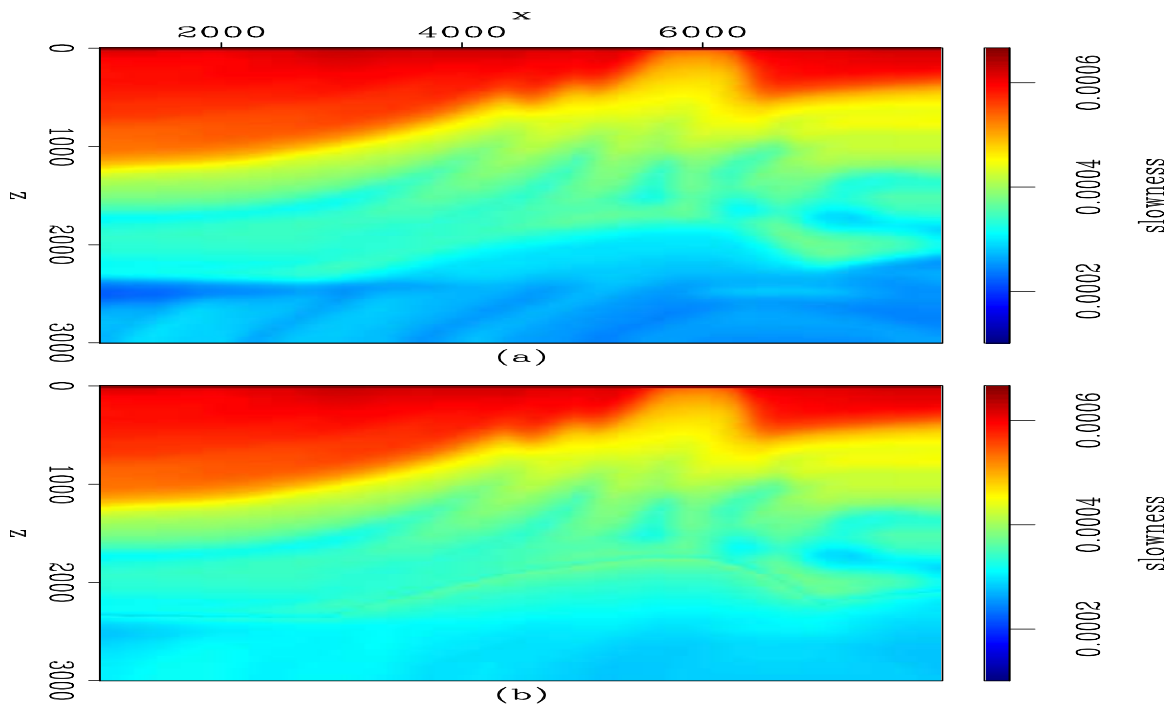


Figure 1: a) Correct slowness; b) Background slowness.

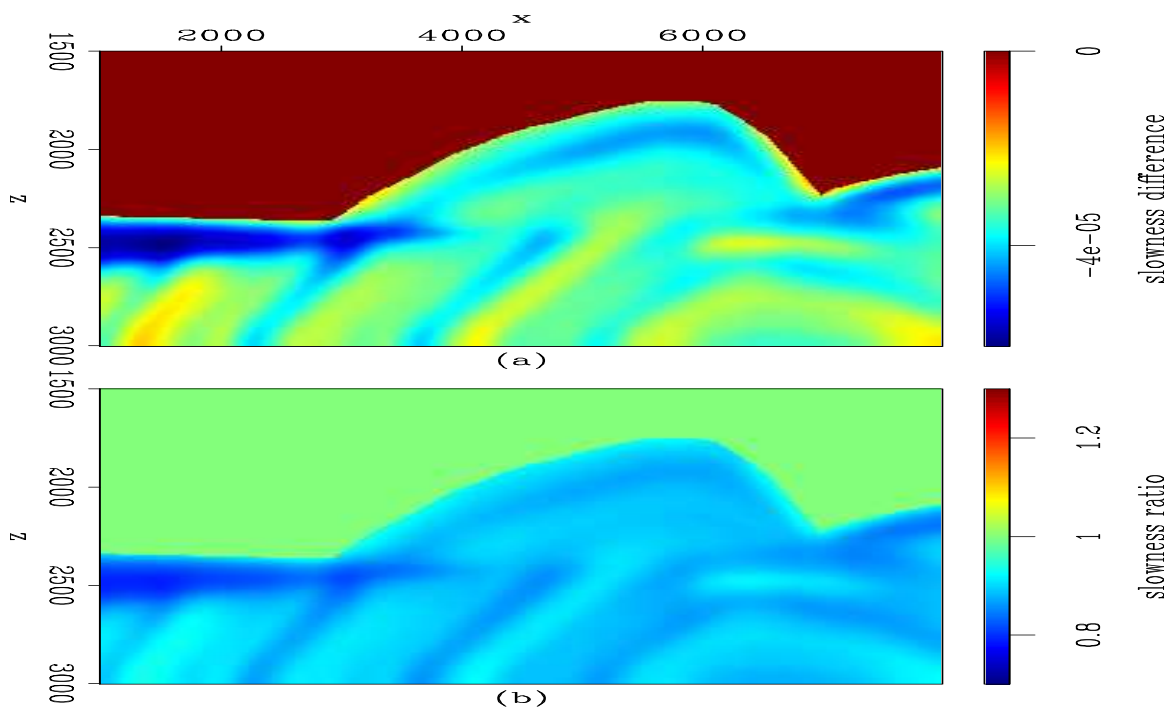


Figure 2: a) Slowness perturbation; b) Slowness ratio.

the initial conditions to model the image-space phase-encoded data, as discussed by Biondi (2006, 2007). Figure 4 shows the initial conditions for the prestack modeling. Figure 4(a) shows the initial condition for modeling the receiver wavefield, and Figure 4(b) shows the initial condition for modeling the source wavefield.

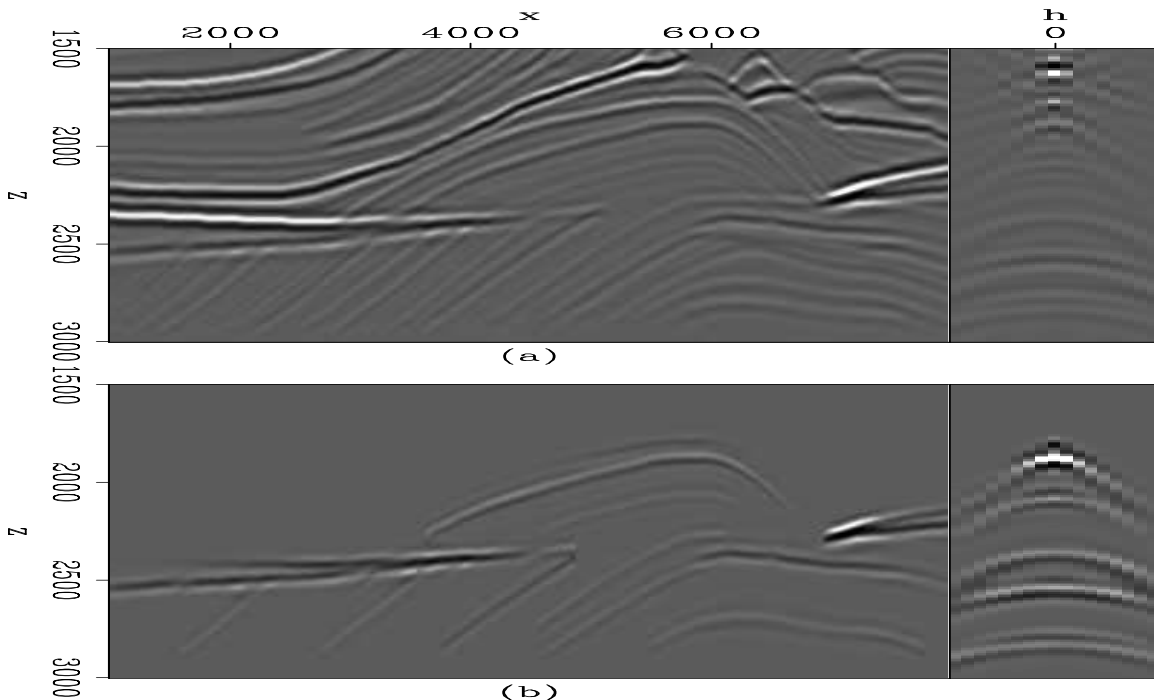


Figure 3: a) Background image; b) Windowed image used to compute image-space-encoded data.

Two image-space phase-encoded data sets were synthesized using different parameters. One contains one random realization of areal shots initiated simultaneously at every 11th CMP position (264 m) and encoded according to the CMP position and reflector number, generating 11 areal shot gathers. The other data set corresponds to two random realizations modeled with SODCIG sampling interval of 840 m, composed of 70 areal shot gathers. Because in the velocity inversion we consider the maximum subsurface offset to be 192 m, this data set is expected to generate less crosstalk. In some comparisons, we use just one random realization (35 areal shots) of the second data set. We use the two random realizations when comparing the results of the non-linear optimization of the slowness model.

In the slowness optimization problem, we compute the image perturbation by applying the DSO operator,  $\mathbf{O}$ , to the background image in the subsurface-offset domain. The corresponding objective functional is

$$J = \frac{1}{2} \|\mathbf{O}\hat{\mathbf{I}}\|^2 = \frac{1}{2} \|h\hat{\mathbf{I}}\|^2. \quad (16)$$

Since the DSO operator is independent of the slowness, the gradient of  $J$  with respect

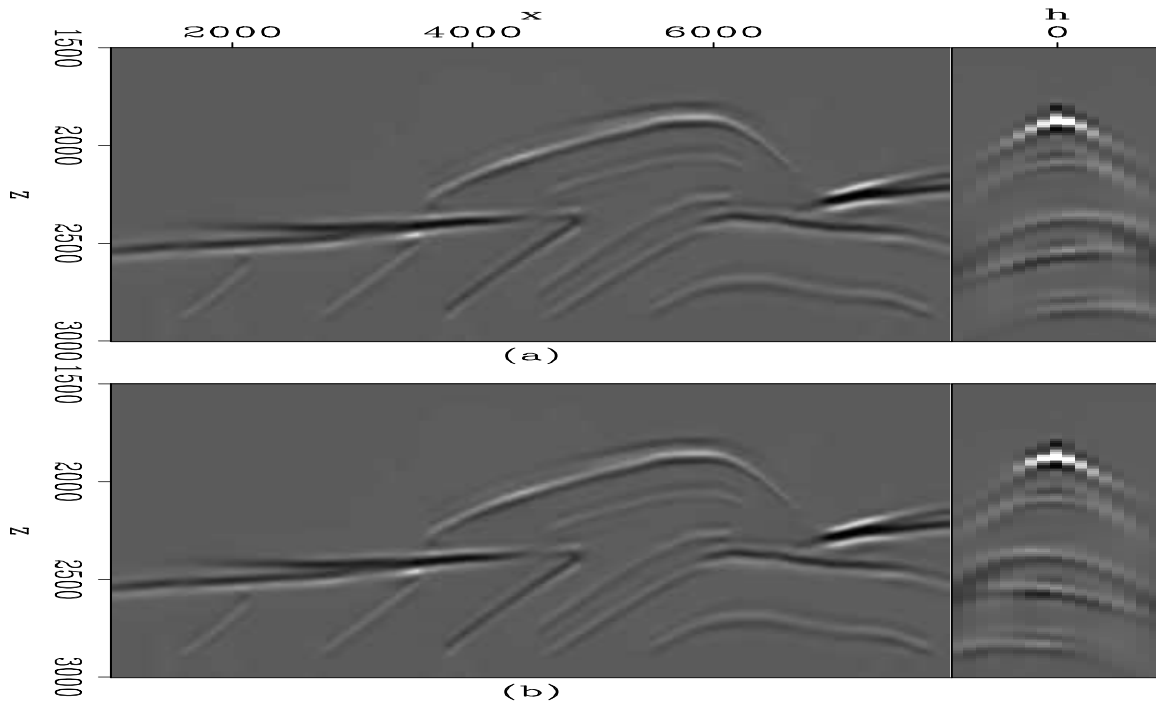


Figure 4: a) Initial condition for modeling the receiver wavefield. b) Initial condition for modeling the source wavefield.

to the slowness  $\mathbf{s}$  is

$$\nabla J = \left( \frac{\partial \mathbf{I}}{\partial \mathbf{s}} \Big|_{\mathbf{s}=\hat{\mathbf{s}}} \right)^* \mathbf{O}^* \mathbf{O} \hat{\mathbf{I}} = \mathbf{T}^* \mathbf{O}^* \mathbf{O} \hat{\mathbf{I}}. \quad (17)$$

Given that the computation of the DSO objective functional is fully automated, it can be minimized by using quasi-Newton methods. Here, we specifically use the constrained L-BFGS algorithm (Nocedal and Wright, 2000).

To guarantee smoothness of the wave-equation tomography gradient, we use a B-spline representation according to a grid of 960 m in the  $x$ -direction and 16 m in the  $z$ -direction.

In the following, we compare the results of applying the forward and adjoint wave-equation tomography operators using the original shot gathers and the image-space phase-encoded gathers. We also solve the optimization problem and evaluate the accuracy of the results by comparing the optimized slowness models with the true slowness model, and also by comparing migrated images of the 376 original shot gathers with the true slowness model and with the predicted slownesses.

Figure 5 shows the image perturbation computed by applying the forward tomographic operator,  $\mathbf{T}$ , and using the background slowness of Figure 1(b) and the known slowness perturbation of Figure 2. Figure 5a shows the image perturbation computed in the shot-profile domain for the 376 shots; Figure 5b shows the image

perturbation computed in the image-space phase-encoded domain using 11 image-space phase-encoded gathers; and Figure 5c shows the image perturbation computed in the image-space phase-encoded domain using 35 image-space phase-encoded gathers. Notice that the dispersed crosstalk is stronger in Figure 5b than in Figure 5c.

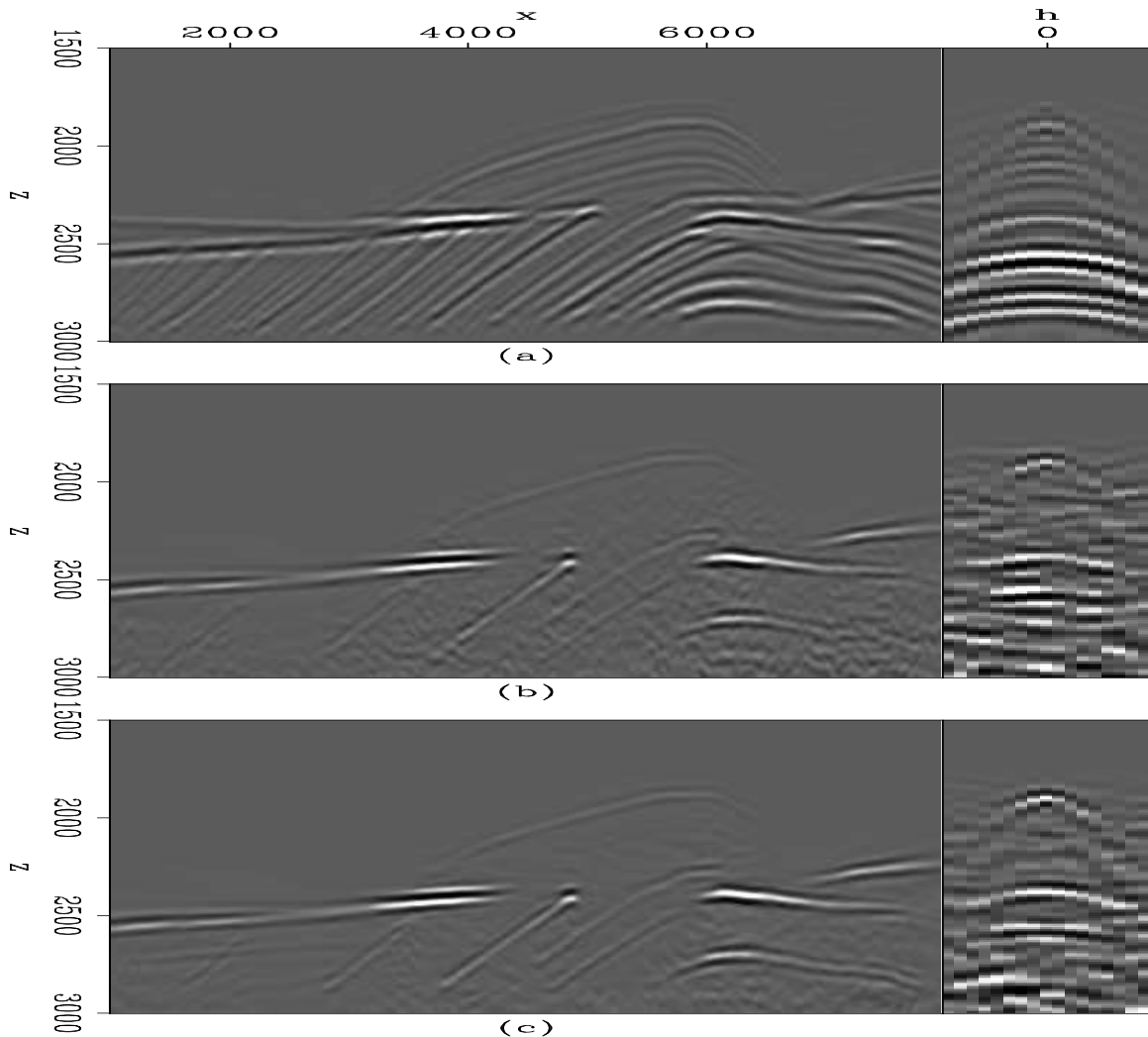


Figure 5: a) Image perturbation in the shot-profile domain; b) Image perturbation computed with 11 image-space phase-encoded wavefields; c) Image perturbation computed with 35 image-space phase-encoded wavefields.

Figure 6 illustrates the normalized slowness perturbations obtained by applying the adjoint tomographic operator  $\mathbf{T}^*$  to the image perturbations of Figure 5. Compare with the correct slowness perturbation of Figure 2. Figure 6a is the predicted slowness perturbation found by back-projecting Figure 5a using all 376 shot gathers; Figure 6b shows the back-projection of Figure 5b using 11 image-space phase-encoded gathers; and Figure 6c shows the back-projection of Figure 5c using 35 image-space phase-encoded gathers. Notice that we do not use a B-spline representation for the

slowness perturbations. In general, the predicted slowness perturbation with image-space phase-encoded gathers shows a structure similar to that obtained with the original shot gathers. The differences can be credited, at first order, to the occurrence of residual crosstalk in the image-space phase-encoded perturbed image and to a sub-optimal number of selected reflectors for the prestack exploding-reflector modeling.

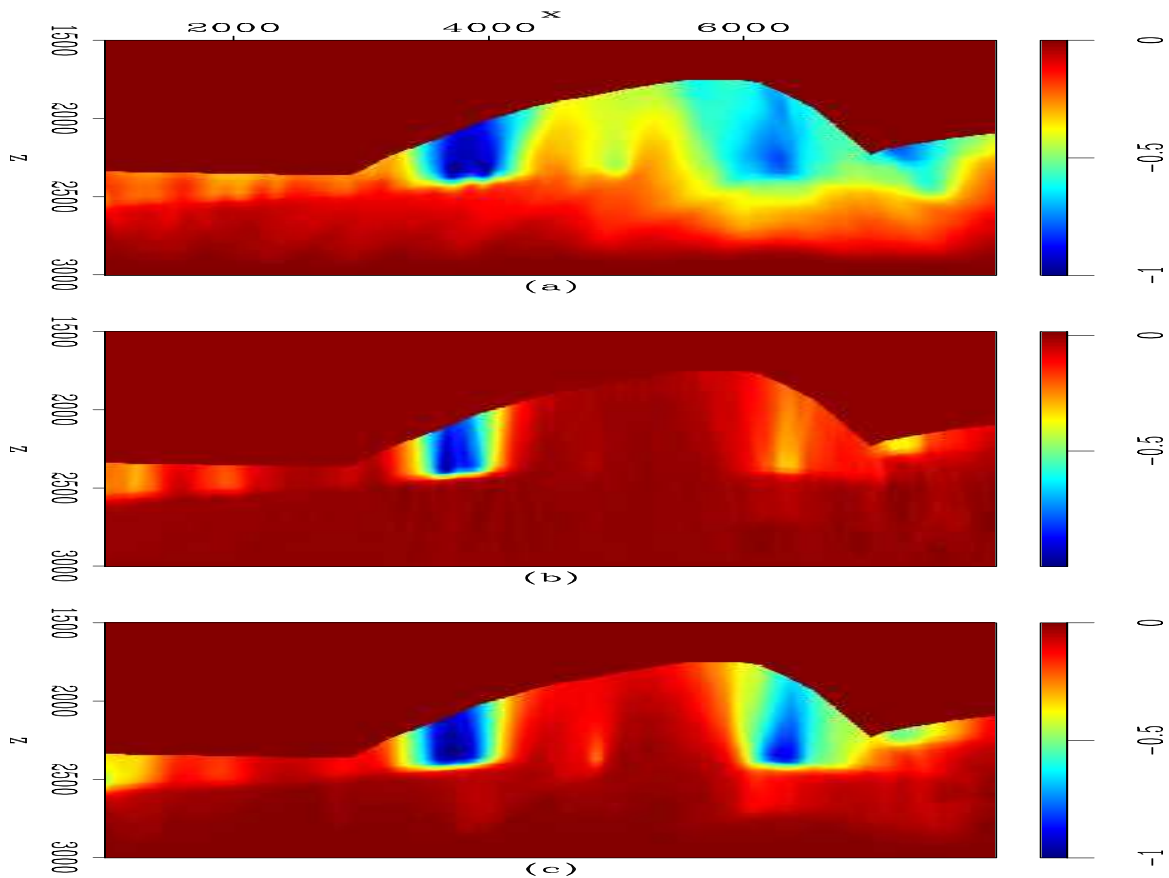


Figure 6: Normalized slowness perturbation obtained by applying the adjoint tomographic operator  $\mathbf{T}^*$  on the image perturbations in Figure 5. a) Slowness perturbation computed from Figure 5a. b) Slowness perturbation computed from Figure 5b. c) Slowness perturbation computed from Figure 5c.

Finally, we compare the optimized slowness models with the correct slowness model of Figure 1(a). We computed 3 non-linear iterations with a total of 15 function evaluations for both the 11-gather image-space phase-encoded data set and 35 areal shots (one random realization) of the 70-gather image-space phase-encoded data set; we also computed 2 non-linear iterations with a total of 6 function evaluations using the two random realizations of the 70-gather image-space phase-encoded data set. To verify the accuracy of the resulting optimized slowness models, we also migrated the original shot gathers with the three optimized slownesses and also with the correct slowness.

Figure 7 shows the optimized slownesses and, for comparison purposes, the true slowness. Figure 7(a) displays the slowness model; Figure 7(b) is the slowness model obtained with the 11-gather image-space phase encoded data; Figure 7(c) is the slowness model obtained with the 35-gather image-space phase encoded data; and Figure 7(d) is the slowness model obtained with the 70-gather image-space phase encoded data. In general, the predicted slownesses are reasonable. The predicted slowness using the 11 image-space phase-encoded gathers, however, presents slightly lower values than the other two predicted slownesses. Notice that the detailed slowness variation present in the true slowness is not recovered in the optimized slownesses, due to the B-spline representation of the gradient of the wave-equation tomography objective functional. However, the slowness model obtained with the 70 image-space phase encoded gathers recovers the low slowness values on the left of model better than the other two predicted slownesses.

Figure 8 shows the ratio between the true slowness and the predicted slownesses. Figure 8(a) shows the slowness ratio for the predicted slowness obtained with the 11 image-space phase-encoded gathers; Figure 8(b) shows the slowness ratio for the predicted slowness is obtained with the 35 image-space phase-encoded gathers; and Figure 8(c) shows the slowness ratio for the predicted slowness is obtained with the 70 image-space phase-encoded gathers. Compare these figures with Figure 1(b).

Figure 9 displays the zero-subsurface-offset section after migration of the 376 original shot gathers using the true slowness model (Figure 9(b)), the predicted slowness using 11 image-space phase encoded gathers (Figure 9(c)), the predicted slowness using 35 image-space phase encoded gathers (Figure 9(d)), and the predicted slowness using 70 image-space phase encoded gathers (Figure 9(e)). For comparison, we also display in Figure 9(a) the zero-subsurface-offset section after migration with the background slowness of Figure 1(b). From top to bottom, Figure 10 displays SODCIGs at 1500 m, 3500 m, 5500 m and 7500 m after migration of the 376 original shot gathers, using the background slowness of Figure 1(b) in the first row, using the true slowness model in the second row, using the predicted slowness with 11 image-space phase encoded gathers in the third row, using the predicted slowness with 35 image-space phase encoded gathers in the fourth row, and using the predicted slowness with 70 image-space phase encoded gathers in the fifth row. The subsurface-offset ranges from -192 m to 192 m. In Figure 9(b), the reflector at (4000 m, 2500 m) is pushed down and the reflector at (7000 m, 2600 m) is not as flat as in Figure 9(a) and (d). In addition, the SODCIGs in Figure 10 show better focusing when more image-space phase-encoded gathers are used in the wave-equation tomography.

The accuracy of the optimized slowness improves when using more phase-encoded gathers in the wave-equation tomography, or, in other words, when the crosstalk in the perturbed image is less severe, as Figures 5 and 6 suggest. Figure 11 shows the perturbed image computed by applying the DSO operator onto the image migrated with the background slowness of Figure 1(b). The panel on the left corresponds to the subsurface-offset -144 m and the panel on the right is the SODCIG taken at 5500 m. Figure 11(a) shows the perturbed image using 11 image-space phase-

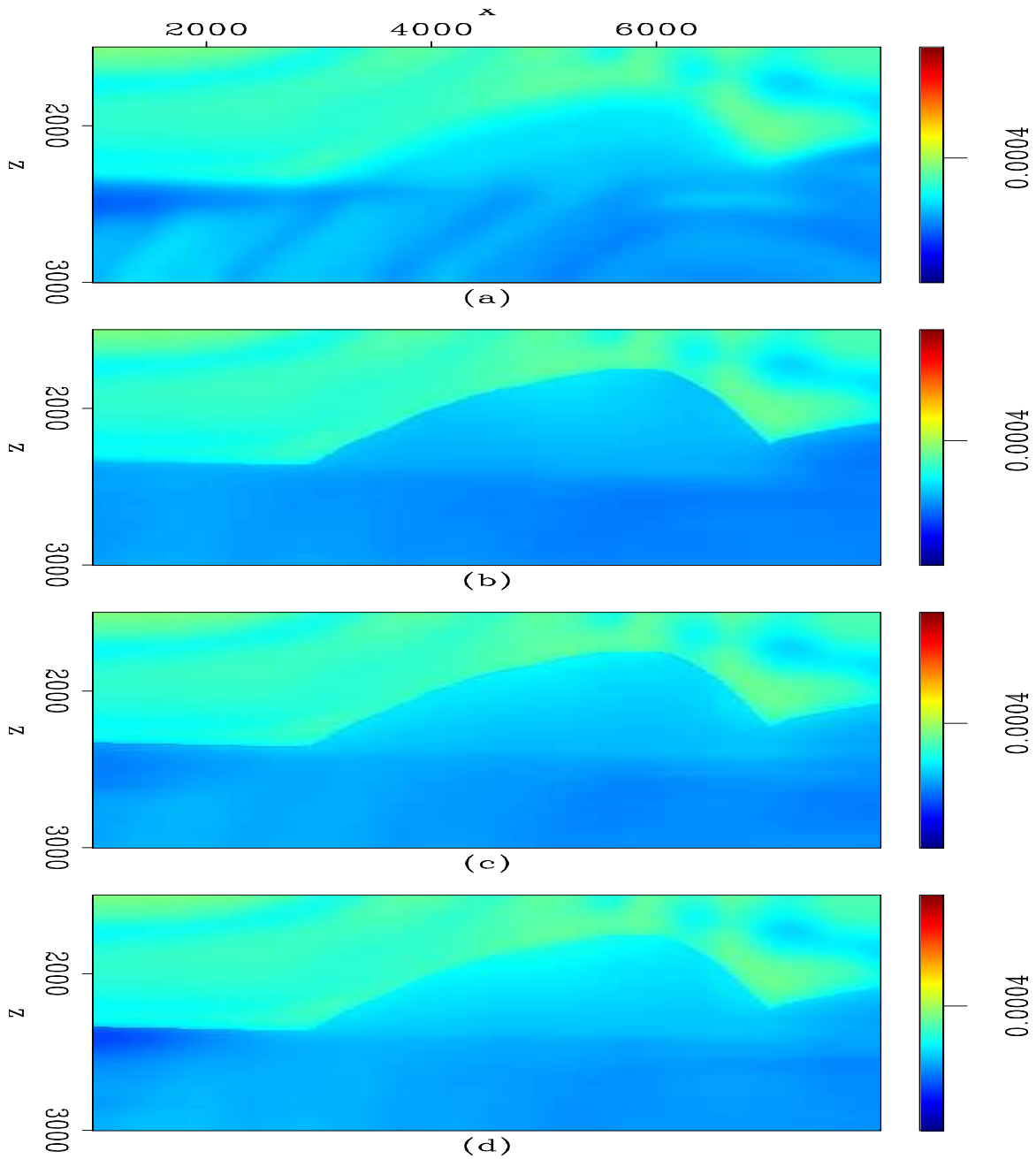


Figure 7: True and optimized slownesses. a) True slowness model; b) Slowness model obtained with the 11-gather image-space phase-encoded data. c) Slowness model obtained with the 35-gather image-space phase-encoded data. d) Slowness model obtained with the 70-gather image-space phase-encoded data.

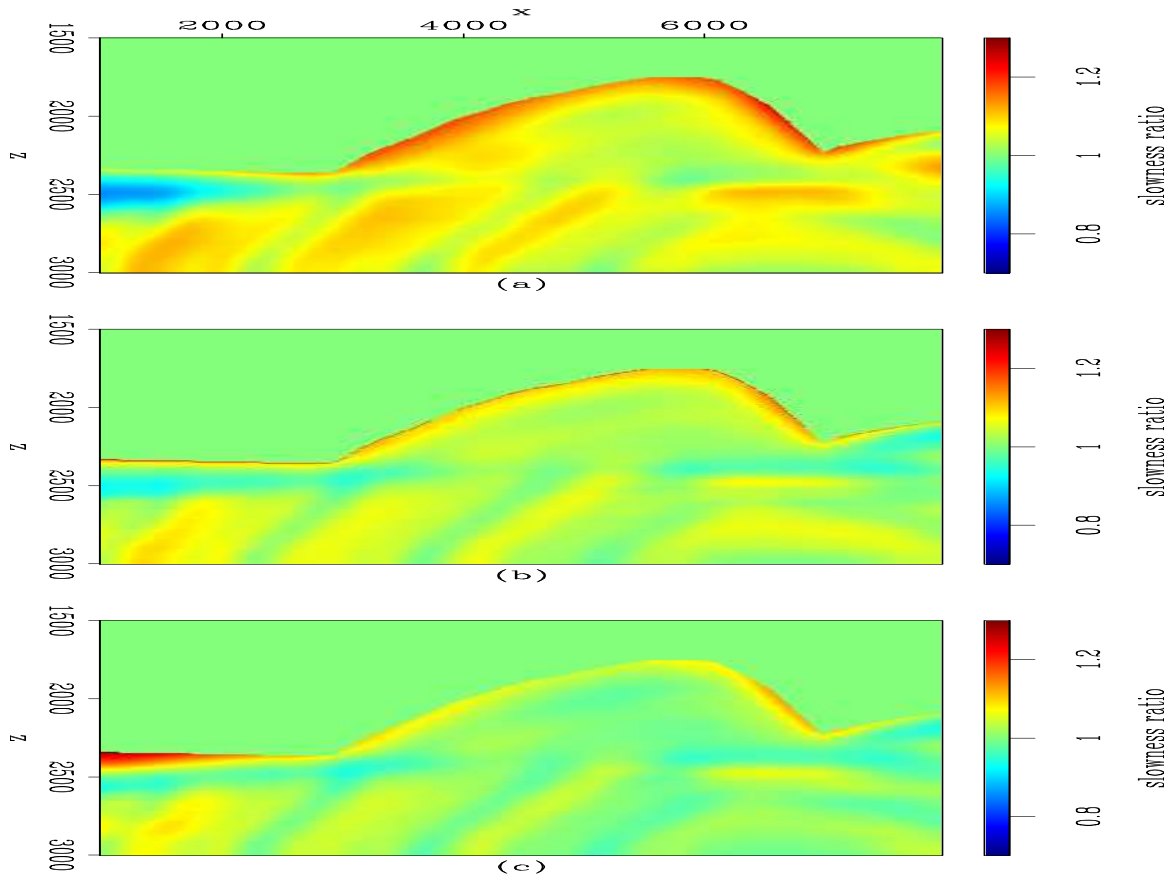


Figure 8: Ratio between true slowness and the optimized slownesses of Figure 7. a) Slowness ratio obtained with the 11-gather image-space phase-encoded data. b) Slowness ratio obtained with the 35-gather image-space phase-encoded data. c) Slowness ratio obtained with the 70-gather image-space phase-encoded data.

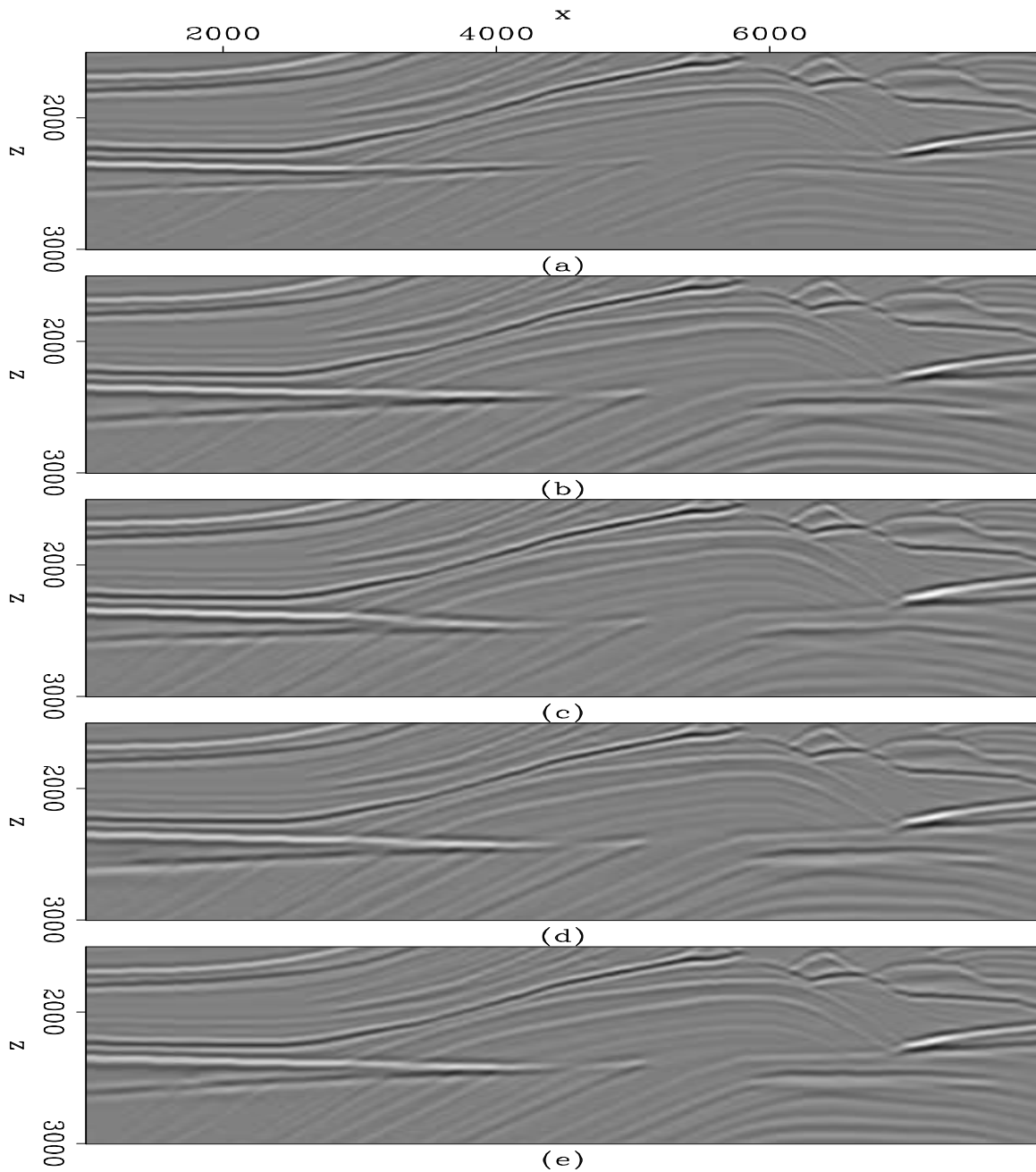


Figure 9: Zero-subsurface-offset section after migration of the 376 original shot gathers using: a) the true slowness model; b) the predicted slowness model of Figure 7(a); c) the predicted slowness model of Figure 7(b); and d) the predicted slowness model of Figure 7(c).

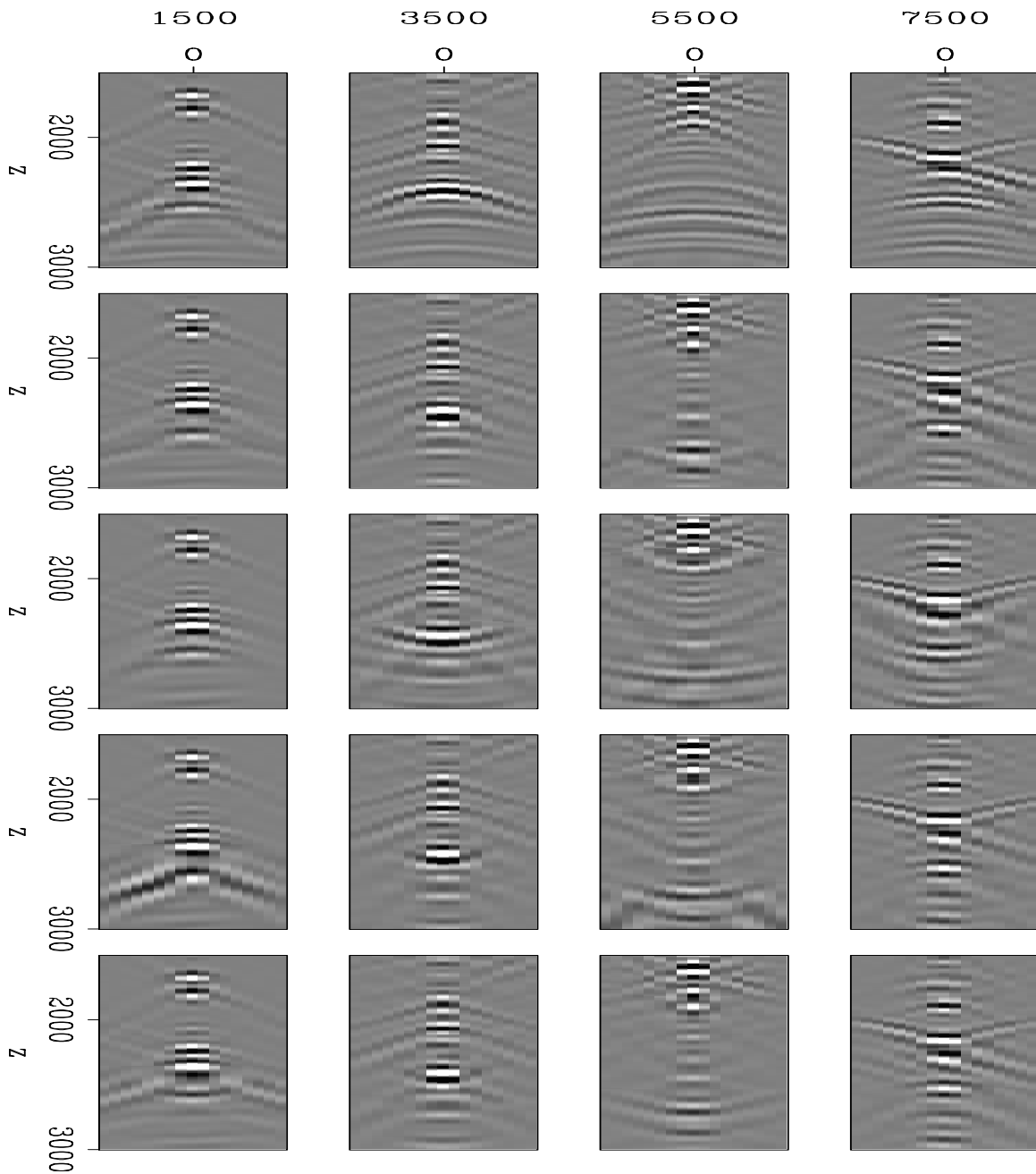


Figure 10: Subsurface-offset gathers after migration of the 376 original shot gathers. From top to bottom: in the first row, using the background slowness model; the second row, using the true slowness model; in the third row, using the predicted slowness model of Figure 7(b); in the fourth row, using the predicted slowness model of Figure 7(c); and in the fifth row, using the predicted slowness model of Figure 7(d).

encoded gathers; Figure 11(b) shows the perturbed image using 35 image-space phase-encoded gathers; and Figure 11(c) shows the perturbed image using 70 image-space phase-encoded gathers. Notice how the signal-to-noise ratio improves as more phase-encoded gathers are used. The SODCIG of the perturbed image of Figure 11(a) presents coherent events, related to unattenuated crosstalk, curving upward at  $z = 2700$  m; these events are not present in Figures 11(b) and (c). If these events are sufficiently incoherent along the subsurface-offset sections, a two-dimensional filter could be applied to attenuate them. In that case, a new objective function should be defined. This deserves future investigation.

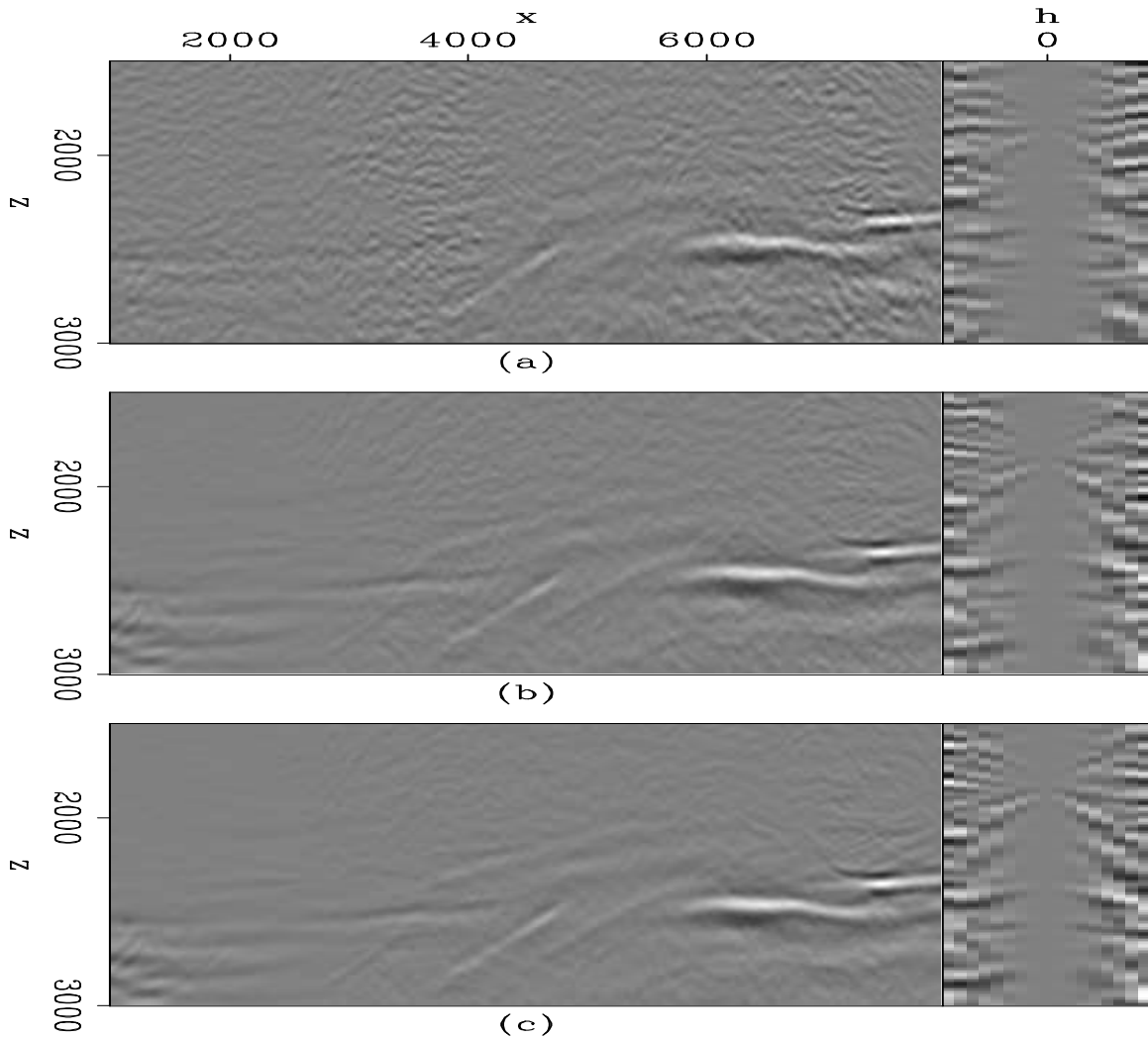


Figure 11: Perturbed images computed with the DSO operator. a) Perturbed image using 11 image-space phase-encoded gathers. b) Perturbed image using 35 image-space phase-encoded gathers. c) Perturbed image using 70 image-space phase-encoded gathers.

## CONCLUSIONS

We present a cost-effective method to perform image-space wave-equation tomography using image-space phase-encoded shot gathers. One important advantage is that we are able to synthesize a much smaller data set while still keeping necessary velocity information for migration velocity analysis; hence the computational cost of performing image-space wave-equation tomography can be significantly reduced. Our results show that using the image-space phase-encoded wavefields provides a gradient of the tomography objective functional similar to that computed using the original shot gathers, but at significantly lower cost. We also show that the accuracy of optimized slowness depends on the amount of residual crosstalk in the perturbed image.

## REFERENCES

- Biondi, B., 2006, Prestack exploding-reflectors modeling for migration velocity analysis: 76th Ann. Internat. Mtg., Expanded Abstracts, 3056–3060, Soc. of Expl. Geophys.
- , 2007, Prestack modeling of image events for migration velocity analysis: **SEP-131**, 101–118.
- , 2008, Automatic wave-equation migration velocity analysis: **SEP-134**, 65–78.
- Biondi, B. and P. Sava, 1999, Wave-equation migration velocity analysis: 69th Ann. Internat. Mtg., Expanded Abstracts, 1723–1726, Soc. of Expl. Geophys.
- Claerbout, J. F., 1971, Towards a unified theory of reflector mapping: *Geophysics*, **36**, 467–481.
- Guerra, C. and B. Biondi, 2008, Prestack exploding reflector modeling: The crosstalk problem: **SEP-134**, 79–92.
- Jiao, J., D. R. Lowrey, J. F. Willis, and R. D. Martínez, 2008, Practical approaches for subsalt velocity model building: *Geophysics*, **73**, VE183–VE194.
- Kosloff, D., J. Sherwood, Z. Koren, E. Machet, and Y. Falkovitz, 1996, Velocity and interface depth determination by tomography of depth migrated gathers: *Geophysics*, **61**, 1511–1523.
- Nocedal, J. and S. Wright, 2000, *Numerical optimization*: Springer Verlag, New York.
- Romero, L. A., D. C. Ghiglia, C. C. Ober, and S. A. Morton, 2000, Phase encoding of shot records in prestack migration: *Geophysics*, **65**, 426–436.
- Sava, P., 2004, *Migration and Velocity Analysis by Wavefield Extrapolation*: PhD thesis, Stanford University.
- Shen, P., 2004, *Wave-equation Migration Velocity Analysis by Differential Semblance Optimization*: PhD thesis, Rice University.
- Shen, P. and W. W. Symes, 2008, Automatic velocity analysis via shot profile migration: *Geophysics*, **73**, VE49–VE59.
- Stork, C., 1992, Reflection tomography in the postmigrated domain: *Geophysics*, **57**, 680–692.
- Tang, Y., C. Guerra, and B. Biondi, 2008, Image-space wave-equation tomography in the generalized source domain: **SEP-136**, 1–22.

- Tarantola, A., 1987, Inverse problem theory: Methods for data fitting and model parameter estimation: Elsevier.
- Vigh, D. and E. W. Starr, 2008, 3d prestack plane-wave, full-waveform inversion: *Geophysics*, **73**, VE135–VE144.
- Whitmore, N. D., 1995, An Imaging Hierarchy for Common Angle Plane Wave Seismogram: PhD thesis, University of Tulsa.
- Woodward, M. J., 1992, Wave-equation tomography: *Geophysics*, **57**, 15–26.